PAPER

Optimizing transmittance in WO₃-based electrochromic films: advanced growth control *via* chemical bath deposition

Jiacheng Yao, [ID] *[a] Gai Lin[a] and Min Zhang*[b]

Tungsten trioxide (WO₃)-based electrochromic film is a promising component for all-solid-state electrochromic devices, which can be used in smart windows to control the indoor temperature and incident solar irradiation. However, its practical application suffers from significant challenges including slow switching kinetics, low cycling stability, and high production costs. To overcome these limitations, a mild chemical bath deposition approach is introduced. Through strategic control of reactants, the thickness of the WO₃ film and the constituent WO₃ nanosheets forming the film can both be systematically regulated. The optimized W₂ sample demonstrates remarkable electrochromic performance, achieving an optical modulation amplitude of $\Delta T = 67.85\%$ at 620 nm along with good cycling stability, which was caused by its well-engineered hierarchical structure featuring a thin film configuration (430 nm) composed of ultrathin nanosheets (39.48 nm). This work points out a new strategy for modulating the optical properties of WO₃ electrochromic film through reactant control during a chemical bath deposition process, providing valuable insights for the rational design of high-performance smart windows.

1 Introduction

In the 21st century, energy and the environment are the most concerning issues for all people worldwide. Among all energy consumption fields, buildings consume about 20–40% of the world's energy generation, which is mainly through heating, ventilation, air conditioning (HVAC) systems and lighting systems.[1–3] As a promising solution, smart windows can inhibit the transmission of visible and infrared light in summer, thereby reducing the energy consumption of HVAC systems. The electrochromic device (ECD) is an important part of smart windows, which is combined with a conducting transparent conductive electrode (TCE), electrochromic layer, electrolyte, and ion-storage layer.[2,4–13] While all components have been systematically investigated, the electrochromic layer remains the most visually distinctive element due to its reversible optical transitions. This unique characteristic stems from electrochemical redox reactions that induce controllable variations in light absorption spectra under applied electrical potentials.

WO₃ is one of the most extensively studied electrochromic materials and currently the sole commercially implemented option for smart window applications.[14–18] This transition metal oxide exhibits reversible optical switching behavior, transitioning to a blue-colored state under cathodic polarization while recovering optical transparency upon anodic polarization. Notably, this electrochromic performance is critically dependent on the nanoscale thickness and crystalline microstructure of the electrochromic layer.[5,7,8,12,13,19–21]

Previous studies have revealed that exceeding 1 μm in thickness induces irreversible structural modifications, manifested by yellow or white coloration and a deterioration in visible light transmittance.[13,20,22–29]

In previous works, many methods have been used to fabricate WO₃ electrochromic films under 1 μm. Compared with traditional sol–gel, sputtering, and hydrothermal methods, the chemical bath deposition method has been favored for its low cost and process temperature and structural control. Though the chemical bath method has been used in some previous reports, the obtained samples showed unsatisfactory performance, especially for the optical modulation amplitude.[30–35]

Building upon our prior study, a WO₃ film was fabricated on SnO₂:F (FTO) glass by a chemical bath method. In this work, the growth processes were further investigated and an *in situ* electrochromic test was carried out to evaluate the electrochromic properties.

2 Experimental

2.1 Chemicals

Sodium tungsten oxide dihydrate (Na₂WO₄·2H₂O) and oxalic acid (H₂C₂O₄) were purchased from Aladdin Chemicals Co.

[a] Jiangsu Urban and Rural Construction Vocational College, Changzhou, Jiangsu, China. E-mail: jcyao0415@foxmail.com

[b] College of Chemical and Material Engineering, Quzhou University, Quzhou, Zhejiang, China. E-mail: mzhang.chemmater@qzc.edu.cn

Hydrochloric acid (HCl) was purchased from Sinopharm Chemical Reagent Co. Ltd. All chemicals were used without any further purification. FTO glass with a sheet resistance of 14–16 Ω sq^{-1} was obtained from Zhuhai Kaivo Optoelectronic Technology Co., and was cut into a size of 1 cm $\times$ 5 cm. This was cleaned by sonication with acetone, ethanol and DI water in sequence before use.

2.2 Synthesis of H_2WO_4 film on FTO

Solution A was prepared by dissolving 6.6 g $Na_2WO_4 \cdot 2H_2O$ in 100 mL deionized water (DI water). Solution B was formulated by dissolving 3.6 g of $H_2C_2O_4$ in 100 mL DI water. For the chemical bath deposition, 0.5 mL of both solution A and B were transferred to a 12 mL polypropylene centrifuge tube. The mixture was diluted to 3 mL with DI water, followed by addition of 2 mL HCl (2 M) to achieve a final pH < 1. The FTO glass was positioned in the reaction tube with the conductive surface facing downward against the tube wall. The sealed reaction system was kept in a preheated metal heating block maintained at 60 °C for 3 h. After the reaction time, the synthesized H_2WO_4/FTO samples were taken out immediately and rinsed with DI water and ethanol several times to remove the residual reactants. Then it was dried at 60 °C for 12 h and marked as H_5. Thermal conversion to WO_3/FTO was achieved through calcination in a muffle furnace at 500 °C for 3 h, inducing a chromatic transition from light yellow to pale white; the annealed specimen was labeled as W_5 (Fig. 1). A series of samples was fabricated by similar steps except for systematically varying the volume of solution B; these were named H_1 to H_9 before annealing and W_1 to W_9 after annealing. Full parametric details are shown in Table S1 in the SI.

2.3 Characterization

The structure of the as-prepared H_2WO_4/FTO and WO_3/FTO samples were characterized by XRD (SmartLab SE, Rigaku, Japan) using a Cu Kα radiation (λ = 0.15418 nm) over a 2θ range from 10° to 70° at a scan rate of 10° min^{-1}. The morphology and microstructure were observed using a scanning electron microscope (FESEM, GeminiSEM 360, ZEISS, Germany). The bonding configurations and charge transfer process of the products were determined with X-ray photoelectron spectroscopy measurements (XPS, AXIS SUPRA+, SHIMADZU, Japan), the binding energies of the tested elements were adjusted based on the indefinite carbon peak at 284.8 eV. The optical transmittance of the samples was measured using a UV-vis spectrophotometer (N4S, INESA, China). The electrochemical measurements were carried out on an electrochemical workstation (CS2350M, Wuhan Corrtest Instrument, China) using a three-electrode system consisting of a standard Ag/AgCl electrode as the reference electrode (RE), a platinum plate as the counter electrode (CE) and the fabricated WO_3/FTO as the working electrode (WE) in 0.5 M H_2SO_4. The in situ electrochromic test was carried out by combing the spectrophotometer and electrochemical workstation above. It was carried out in a 0.1 M $LiClO_4$/PC with a two-electrode system consisting of a platinum plate as the counter electrode and the as-prepared WO_3/FTO as the working electrode.

3 Results and discussion

3.1 Composition and structure

Fig. 2 displays the XRD patterns of the as-prepared H_2WO_4 and WO_3 samples. As depicted in Fig. 2a, all H series samples matched the H_2WO_4 phase (JCPDS No. 43-0679). A peak at 16.4°, corresponding to the (020) plane, showed an increasing trend from H_1 to H_9. Meanwhile, the peak at 25.6°, associated with the (111) plane, increased from H_1 to H_5 and then decreased. Another notable peak at 34.0°, corresponding to the (200) plane, increased from H_1 to H_6 before decreasing. The varying peak intensities indicated that controlling the addition of $H_2C_2O_4$ altered the preferential growth direction of the H_2WO_4 nanosheets. Our previous research confirmed that the exposed facet of H_2WO_4 nanosheets prepared by this method was the (020) plane. The peaks at 26.4° were attributed to FTO; a higher intensity suggested a thinner H_2WO_4 film. Notably, H_1 and H_9 in Fig. 2a were particularly thin.

In Fig. 2b, all W series samples matched the WO_3 phase (JCPDS No. 43-1035). The three peaks located between 20° to 25° are characteristic peaks of WO_3, indexed to the (002), (020), and (200) planes, respectively. The peak intensity of the (002) plane increased with the addition of $H_2C_2O_4$, reaching its maximum in sample W_5. Another peak, located at 34.1° and indexed to the (202) plane, showed a significant change, peaking in sample W_7. These peak intensities revealed a specific orientation in the as-obtained samples, indicative of a nanosheet morphology rather than bulk, as confirmed by SEM images. Additionally, comparing the peak intensities of H_2WO_4 with those of WO_3 samples, a potential correlation can be inferred. Both the (020) plane of H_2WO_4 and the (002) plane of WO_3 exhibited a growth trend with increasing $H_2C_2O_4$ addition, suggesting that the (002) plane of WO_3 may have transformed from the (020) plane of H_2WO_4. Similarly, the (200) and

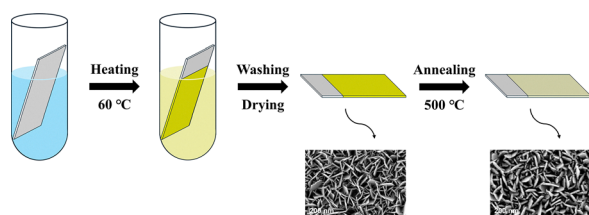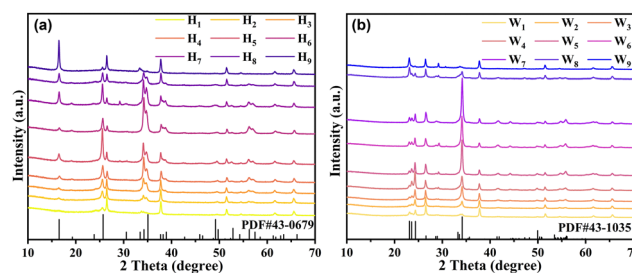Fig. 1 Scheme of preparation route for the WO_3 films.

Fig. 2 XRD patterns of (a) H_1–H_9 samples and (b) W_1–W_9 samples.

(202) planes of WO_3 are likely derived from the (111) and (200) planes of H_2WO_4, respectively.

The top-view SEM images of the as-prepared H_2WO_4 and WO_3 samples are presented in Fig. 3 and 4. Fig. 3 reveals that all samples were composed of numerous nanosheets oriented vertically to the substrate. As the concentration of $H_2C_2O_4$ increased from sample H_1 to H_9, three major changes were observed. Firstly, the surface of the H_2WO_4 film in H_1 was smooth, becoming progressively rougher from H_1 to H_6. For samples H_7, H_8, and H_9, the thin film transitioned into distributed micro–nano islands. Secondly, by measuring 20 random nanosheets (Fig. S2), the average thicknesses of single nanosheets in samples H_1 through H_9 were 25.92, 31.12, 37.65, 49.37, 64.83, 84.62, 78.33, 77.65, and 82.92 nm, respectively. This trend indicates that the thickness of the nanosheets increased with the addition of $H_2C_2O_4$, reaching a stable value around 80 nm. Lastly, the as-prepared H_2WO_4 samples exhibited a square exposed surface, with side lengths increasing from H_1 to H_9. The side length increased from 270 nm for H_1 to 1800 nm for H_9. In Fig. S2, the surface of the H_2WO_4 nanosheets is clearly visible, demonstrating that the thickness of the nanosheet in the H series samples increased with the increasing amount of $H_2C_2O_4$. Additionally, the thicker

nanosheets in H_7, H_8, and H_9 prefer to grow from the surfaces of other nanosheets rather than the FTO substrate.

In our previous work, we successfully achieved the growth of H_2WO_4 nanosheets on various substrates and their self-assembly in solution. The results indicate that Na_2WO_4 hydrolyzes under acidic conditions to form insoluble H_2WO_4 precursors, which preferentially grow at hydrophilic interfaces rich in –OH. Oxalic acid, as a complexing agent, can regulate the hydrolysis rate and nucleation rate of WO_4^- by adjusting its concentration. In short, the higher the concentration of oxalic acid, the more WO_4^- participate in the oxalic acid coordination, resulting in slower hydrolysis and nucleation rates, and thinner nanosheets and thin films being formed.

Fig. 4 illustrates that the morphologies of the WO_3 samples closely resemble those of the H_2WO_4 ones, indicating the high stability of the as-fabricated films under calcination. By measuring 20 random nanosheets from Fig. S4, the thicknesses of samples W_1 through W_9 were determined to be 43.09, 39.48, 48.84, 50.45, 70.79, 82.63, 84.53, 81.25, and 83.34 nm, respectively. The thicknesses of W_4 through W_9 were notably similar to those of H_4 through H_9. However, for W_1, W_2, and W_3, the thicknesses showed a marked increase compared to H_1, H_2, and H_3. From Fig. S4, although the morphologies of the W series samples were analogous to those of the H series, the corners of the WO_3 nanosheets were less sharp than those of the H_2WO_4 nanosheets. Additionally, the surfaces of the WO_3 nanosheets were not as smooth as those of the H_2WO_4 nanosheets. As observed in Fig. S4e, some concavities are present on the surface of the nanosheets, which can be categorized into two types. Point-like pores were caused by stress during the transformation of the crystal structure, resulting in surface breakage on the nanosheet surface. Rod-like pores were attributed to the detachment of nanosheets growing on the primary nanosheet substrate during the annealing process.

The thicknesses of the as-prepared WO_3 films were determined using side-view SEM. Fig. 5 indicates that the FTO layer exhibited a consistent thickness across samples, confirming a uniform test environment. As shown in Fig. 5, sample W_1 exhibited the thinnest thickness, approximately 370 nm. The
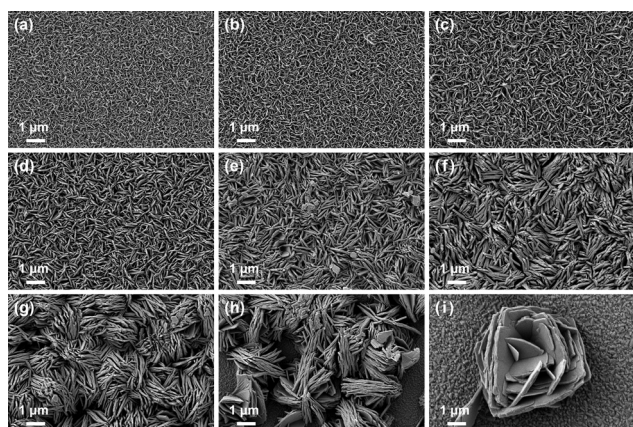

Fig. 3 (a)–(i) SEM images of H_2WO_4/FTO samples (H_1–H_9).
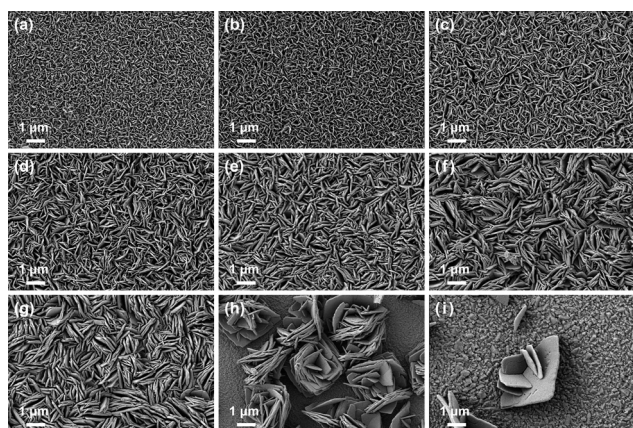

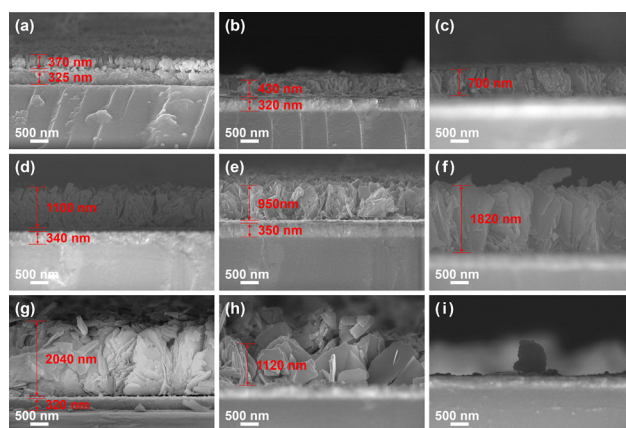**Fig. 4** (a)–(i) SEM images of WO_3/FTO samples (W_1–W_9).

Fig. 5 (a)–(i) Cross section SEM images of WO_3/FTO samples (W_1–W_9).

thickness increased from W_1 to W_7, with the exception of W_5. The W_8 film demonstrated a thickness of 1120 nm. For W_9, given its composition of dispersed micro–nano islands, the film structure could not be discerned in its SEM images. The SEM images further revealed that from W_1 to W_6, the thickness of the WO_3 film was analogous to the length of its constituent nanosheets, suggesting that the film was directly composed of WO_3 nanosheets growing on the FTO substrate. In the case of W_7 and W_8, the film comprised WO_3 nanosheets growing on the FTO substrate and secondary WO_3 nanosheets growing on the primary ones, which contributed to the overall increased thickness of the WO_3 film.

XPS analysis was conducted to investigate the surface chemical composition and the chemical state of each element in the fabricated WO_3 films. Since samples W_1 through W_6 displayed minimal differences in their full-spectrum and high-resolution spectra, only samples W_1, W_7, W_8, and W_9 were selected for further comparison in this section. Fig. 6a reveals characteristic signals for W and O in the full spectra of both samples, confirming the presence of WO_3. However, in W_9, Sn peaks were also detected, attributed to the structure of its dispersed micro–nano islands. As depicted in Fig. 6b, W_1 and W_7 exhibited similar W 4f and W 5p peaks, with a flat region at 27 eV, corresponding to the binding energy of Sn 4d. In W_8, the intensity of the W 4f and W 5p peaks diminished, and a peak emerged at 27 eV. In W_9, the peak at 27 eV was more pronounced, and the W 4f peaks shifted to lower binding energies. This phenomenon indicates a strong interaction between the FTO layer and WO_3, leading to the formation of a heterojunction.

UV-Vis transmittance spectra were employed to assess the optical characteristics of the as-prepared samples. Considering their potential application in smart windows, the samples should exhibit high transmittance in their bleached state. Fig. 7a shows that the FTO-based glass demonstrated high
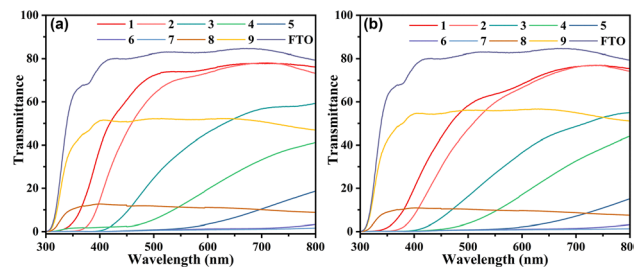

Fig. 7 UV-Vis transmittance spectra of as-prepared (a) H_2WO_4/FTO and (b) WO_3/FTO samples.

transmittance in the visible light region, approximately 80% from 400 to 800 nm. Among all H series samples, H_1 exhibited the highest transmittance, with 77% of incident light passing through from 500 to 800 nm. H_2 displayed a similarly high light transmittance to H_1, with a slight red shift. Subsequently, the light transmittance of the samples decreased with an increase in sample number until H_7. For H_8 and H_9, as the films were not continuous but rather had a distributed micro–nano islands structure, these samples showed a similar transmittance trend in 300 to 800 nm to FTO with a marked decrease in transmittance.

For the WO_3 samples, as shown in Fig. 7b, the UV-vis transmittance spectra revealed a high degree of similarity to those in Fig. 7a. W_1 had the highest transmittance among all W series samples, followed by W_2. The curves for W_3 to W_9 closely matched those of H_3 to H_9, particularly H_8 and H_9. This indicates that in W_3 to W_9, the transmittance of the entire sample was primarily determined by the large thickness of the WO_3 film. In contrast, in W_1 and W_2, the bandgap played the main role in determining transmittance.

3.2 Electrochemical and electrochromic properties

To obtain the electrochemical characteristics of the as-prepared samples, cyclic voltammetry (CV) curves were examined at various scan rates (5, 10, 20, 50, 100 mV s^{-1}) within the potential window of -0.3 V to 0.6 V (vs. Ag/AgCl). Upon application of an initial voltage of -0.3 V, the samples transformed into a dark blue color. As the voltage increased, the electrode materials progressively lightened. With rising scan rates, the anodic peak shifted to a more positive potential. Concurrently, the area of the curve, indicative of capacitance, broadened. This capacitive behavior can be attributed to several mechanisms, such as the adsorption of a monolayer of ions onto the electrode surface, surface redox reactions, or ion intercalation without a phase transition. In this context, the redox reaction pertains to the insertion and extraction of H$^+$ ions and electrons within the WO_3 matrix, resulting in a reversible change in transmittance between blue and yellow states as follows:
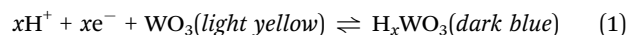
$$x\mathrm{H}^+ + x\mathrm{e}^- + \mathrm{WO_3}(light\ yellow) \rightleftharpoons \mathrm{H}_x\mathrm{WO_3}(dark\ blue) \quad (1)$$

Fig. 8a–i demonstrate that samples W_1 and W_2 exhibit significantly enhanced current and larger voltammogram areas compared to W_3, W_4, and W_5. This indicates a pronounced electrochemical
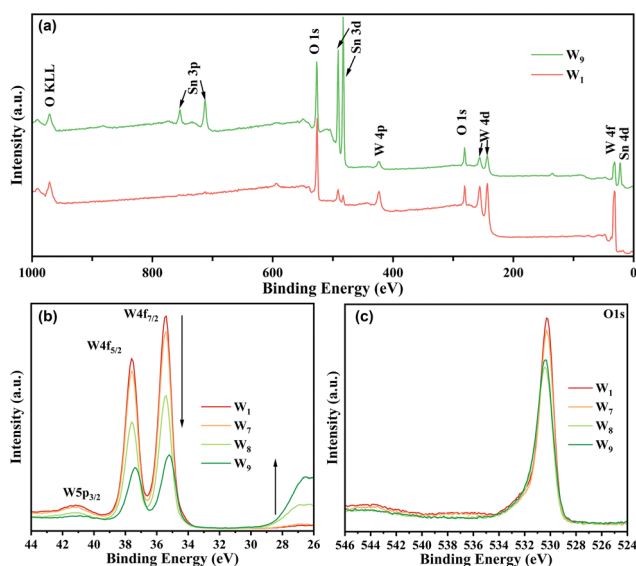

Fig. 6 (a) Survey scan XPS spectra of W_1 and W_9, and the high-resolution XPS spectra for (b) W 4f and (c) O 1s of W_1, W_7, W_8 and W_9.
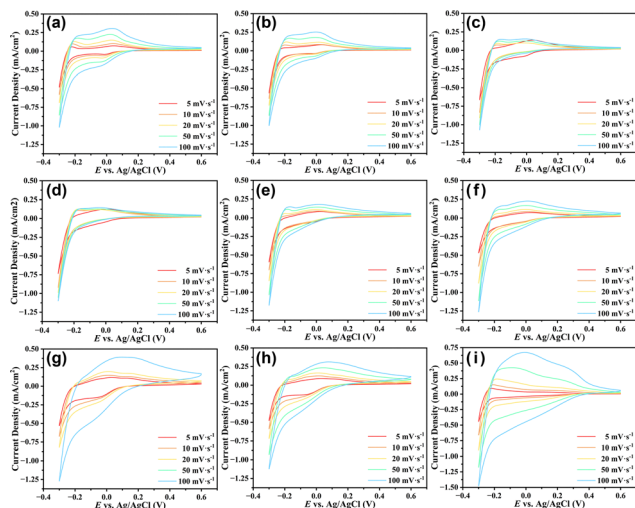
Fig. 8 (a)–(i) The cyclic voltammetry of W_1–W_9 under different scan rates.

Fig. 10 *In situ* UV-vis spectra of (a) W_1, (b) W_2, (c) W_3, (d) W_4, (e) W_5 and (f) W_9.

activity and ion storage capacity during the electrochromic process. These observations are attributed to the rapid charge transfer kinetics and low internal resistance, which stem from the thin nanosheet and film thicknesses. However, although samples W_6, W_7, W_8, and W_9 also show large voltammogram areas, these samples experienced damage during the test which was also shown in Fig. 10 after *in situ* UV-vis transmittance testing. The increased voltammogram areas are ascribed to the electrochemical performance of the FTO matrix.

To directly examine the electrochromic properties of WO_3 films, *in situ* UV-vis spectrometry was employed. The setup for the *in situ* system is shown in Fig. 9. For these tests, a 0.1 M $LiClO_4$/propylene carbonate (PC) solution in a quartz reactor served as a blank. The samples were subjected to a voltage bias sequence of +1.0 V, followed by 0, −0.2, −0.4, −0.6, −0.8, and −1.0 V (*vs.* Ag/AgCl).

Fig. 10 illustrates the electrochromic performance of the W series samples. As a cathodic electrochromic material, the WO_3 film can alternate its color between light yellow and dark blue under a square wave potential ranging from +1.0 V to −1.0 V in a $LiClO_4$/PC solution. Under a negative bias, Li^+ ions are inserted into the crystal lattice of WO_3, causing the film to turn dark blue. Conversely, when a positive bias is applied, Li^+ ions
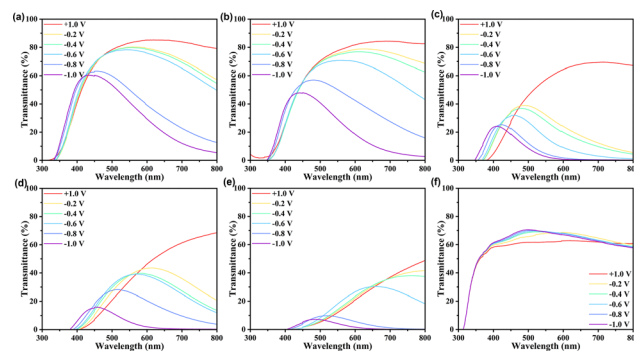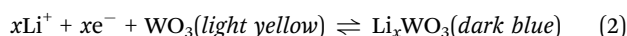
are extracted from the lattice, leading to the film's lightening. The electrochromic reaction can be described as follows:

$$x Li^+ + x e^- + WO_3(light\ yellow) \rightleftharpoons Li_x WO_3(dark\ blue) \quad (2)$$

As shown in Fig. 10, the transmittances at 620 nm in the bleached state (T_b) at a potential of −1.0 V were 86.06%, 82.87%, 66.29%, 50.11%, 24.27%, and 68.40% for samples W_1, W_2, W_3, W_4, W_5, and W_9, respectively. Conversely, the transmittances at 620 nm in the colored state (T_c) at a potential of +1.0 V were 25.09%, 15.02%, 0.55%, 1.32%, 1.04%, and 66.15% for W_1, W_2, W_3, W_4, W_5, and W_9, respectively. For samples W_6, W_7, and W_8, the electrochromic layers were compromised during the coloring process, likely due to lattice expansion associated with the insertion of Li^+ ions. In contrast, the other samples, characterized by thinner single nanosheets and overall electrochromic films, exhibited greater flexibility, which contributed to their resilience against lattice expansion.

The optical images of the as-prepared samples are displayed in Fig. 11. The H series samples exhibited a grayish-green hue, whereas the W series samples turned light yellow after annealing. Following the coloring process, all samples transformed into a blue color. It is evident from the images that samples H_4 to H_8 and W_4 to W_8 exhibited significant haze, as the logos and text beneath the samples were indistinct, rendering them unsuitable for smart window applications. Samples W_1 and W_9, while appearing uniform in the bleached state, demonstrated
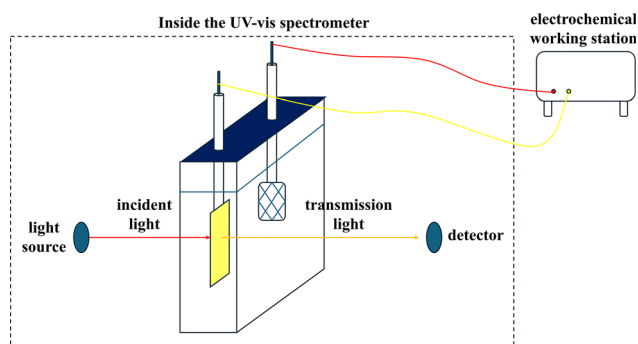

Fig. 9 Scheme of *in situ* transmittance testing system.

Fig. 11 Optical images of as-prepared H_2WO_4/FTO, WO_3/FTO samples and WO_3/FTO samples after coloring.

uneven color distribution in the colored state, revealing their heterogeneous distribution of film thickness.

4 Conclusions

In conclusion, the mild chemical bath deposition method was employed to fabricate WO_3 films on FTO substrates. By controlling the amounts of reactants, the optical properties of the WO_3 films could be effectively modulated. The findings indicate that films with thinner compositions, both in terms of overall thickness and individual nanosheets, result in electrochromic films that are more transparent and flexible. The optimal samples exhibited a high degree of optical modulation, with a transmittance change (ΔT) of 67.85% at 620 nm and demonstrated good cycling stability. Furthermore, the thickness of the electrochromic films could be tuned from 370 nm to 2040 nm, show a viable approach for the large-scale production of WO_3-based smart windows suitable for commercial, tunable electrochromic applications.

Author contributions

J. Y.: concenptualizaion, methodology, investigation, validation, writing – original draft, supervision, funding acquisition; G. L.: methodology, investigation, resources, funding acquisition; M. Z.: methodology, investigation, resources, supervision.

Conflicts of interest

There are no conflicts to declare.

Data availability

The data supporting this article have been included as part of the supplementary information (SI). Supplementary information is available. See DOI: https://doi.org/10.1039/d5ma01024a. Raw data files are available from the corresponding author.

Acknowledgements

Notes and references

1 X. Cao, X. Dai and J. Liu, *Energy Build.*, 2016, **128**, 198–213.
2 U. Berardi, *Resour., Conserv. Recycl.*, 2017, **123**, 230–241.
3 M. González-Torres, L. Pérez-Lombard, J. F. Coronel, I. R. Maestre and D. Yan, *Energy Rep.*, 2022, **8**, 626–637.
4 F. A. Dalenjan, M. Bagheri-Mohagheghi and A. Shirpay, *Opt. Quantum Electron.*, 2022, **54**, 711.
5 J. Guo, H. Jia, Z. Shao, P. Jin and X. Cao, *Acc. Mater. Res.*, 2023, **4**, 438–447.
6 S.-C. Hsu, S.-H. Chao, N.-J. Wu, J.-H. Huang, J.-L. Kang, H. C. Weng and T.-Y. Liu, *J. Alloys Compd.*, 2023, **945**, 169256.
7 Q. Sun, S. Li, X. Yu, Y. Zhang, T. Liu and J. Y. Zheng, *Appl. Surf. Sci.*, 2023, **641**, 158510.
8 S. Yu, J. Yang and C. Song, *ACS Appl. Nano Mater.*, 2023, **6**, 14948–14956.
9 J. Gupta, H. Shaik and S. A. Sattar, *J. Mater. Sci.: Mater. Electron.*, 2024, **35**, 224.
10 K. Usha and S. Y. Lee, *Ceram. Int.*, 2024, **50**, 23244–23255.
11 W. Yong, N. Chen, T. Xiong and G. Fu, *Mater. Today Chem.*, 2024, **38**, 102095.
12 J. Yu, J. Gonzalez-Cobos, F. Dappozze, F. J. Lopez-Tenllado, J. Hidalgo-Carrillo, A. Marinas, P. Vernoux, A. Caravaca and C. Guillard, *Appl. Catal., B*, 2022, **318**, 121843.
13 Y. Chen, J. Sun, Y. Huang, D. Lin, D. Ma and J. Wang, *Ceram. Int.*, 2023, **49**, 29534–29541.
14 J. Y. Zheng, Z. Haider, T. K. Van, A. U. Pawar, M. J. Kang, C. W. Kim and Y. S. Kang, *CrystEngComm*, 2015, **17**, 6070–6093.
15 R. Yu, Z.-H. Meng, M.-D. Ye, Y.-H. Lin, N.-B. Lin, X.-Y. Liu, W.-D. Yu and X.-Y. Liu, *CrystEngComm*, 2015, **17**, 6583–6590.
16 F. Zheng, W. Man, M. Guo, M. Zhang and Q. Zhen, *CrystEngComm*, 2015, **17**, 5440–5450.
17 S. Wang, H. Xu, J. Zhao and Y. Li, *Inorg. Chem. Front.*, 2022, **9**, 514–523.
18 J. Su, L. Chen, C. Xu, Y. Liu, L. Shen and Z. He, *J. Mater. Chem. A*, 2024, **12**, 29383–29401.
19 C. Gao, X. Guo, X. Wu, L.-M. Peng and J. Chen, *Cryst. Growth Des.*, 2023, **23**, 4410–4416.
20 J. Kim, S. Choi, S. Kim, W. Liu, M. Wang, X. Diao and C. S. Lee, *Electrochim. Acta*, 2023, **472**, 143394.
21 J. Yao, P. Li and X. Liu, *J. Cryst. Growth*, 2023, **601**, 126947.
22 C.-M. Chang, Y.-C. Chiang, M.-H. Cheng, S.-H. Lin, W.-B. Jian, J.-T. Chen, Y.-J. Cheng, Y.-R. Ma and K. Tsukagoshi, *Sol. Energy Mater. Sol. Cells*, 2021, **223**, 110960.
23 X. Zhang, S. Dou, W. Li, L. Wang, H. Qu, X. Chen, L. Zhang, Y. Zhao, J. Zhao and Y. Li, *Electrochim. Acta*, 2019, **297**, 223–229.
24 W. Zhang, H. Li, E. Hopmann and A. Y. Elezzabi, *Nanophotonics*, 2020, **10**, 825–850.
25 Z. Wang, X. Wang, S. Cong, J. Chen, H. Sun, Z. Chen, G. Song, F. Geng, Q. Chen and Z. Zhao, *Nat. Commun.*, 2020, **11**, 302.
26 J.-L. Wang, J.-W. Liu, S.-Z. Sheng, Z. He, J. Gao and S.-H. Yu, *Nano Lett.*, 2021, **21**, 9203–9209.
27 B. Zhang, J. Luo, Z. Chen, L. Wu, J. Li, Y. Tian and S. Liu, *J. Electroanal. Chem.*, 2022, **918**, 116487.
28 L. Li, M. Hu, C. Hu, B. Li, S. Zhao, T. Zhou, J. Zhu, M. Liu, L. Li and J. Jiang, *et al.*, *Nano Lett.*, 2023, **23**, 7297–7302.
29 Z. Mei, M. Wang, Y. Ding and X. Diao, *Vacuum*, 2023, **214**, 112219.
30 A. C. Nwanya, C. J. Jafta, P. M. Ejikeme, P. E. Ugwuoke, M. Reddy, R. U. Osuji, K. I. Ozoemena and F. I. Ezema, *Electrochim. Acta*, 2014, **128**, 218–225.

31 M. Z. Najdoski and T. Todorovski, *Mater. Chem. Phys.*, 2007, **104**, 483–487.

32 F. Zhao, Y. Zeng, Z. Cheng, G. Shi, Q. Liu, Y. Liu and G. Han, *Chem. Eng. J.*, 2024, **485**, 149350.

33 S. Wang, T. Jiang, Y. Meng, R. Yang, G. Tan and Y. Long, *Science*, 2021, **374**, 1501–1504.

34 D. Zou, T. Xu, H. Li, X. Zhang, H. Sun, Q. Rao, M. Zhu, S. Chang, Y. He and H. Meng, *ACS Appl. Mater. Interfaces*, 2025, **17**, 21736–21744.

35 P. A. Shinde, V. C. Lokhande, N. R. Chodankar, T. Ji, J. H. Kim and C. D. Lokhande, *J. Colloid Interface Sci.*, 2016, **483**, 261–267.